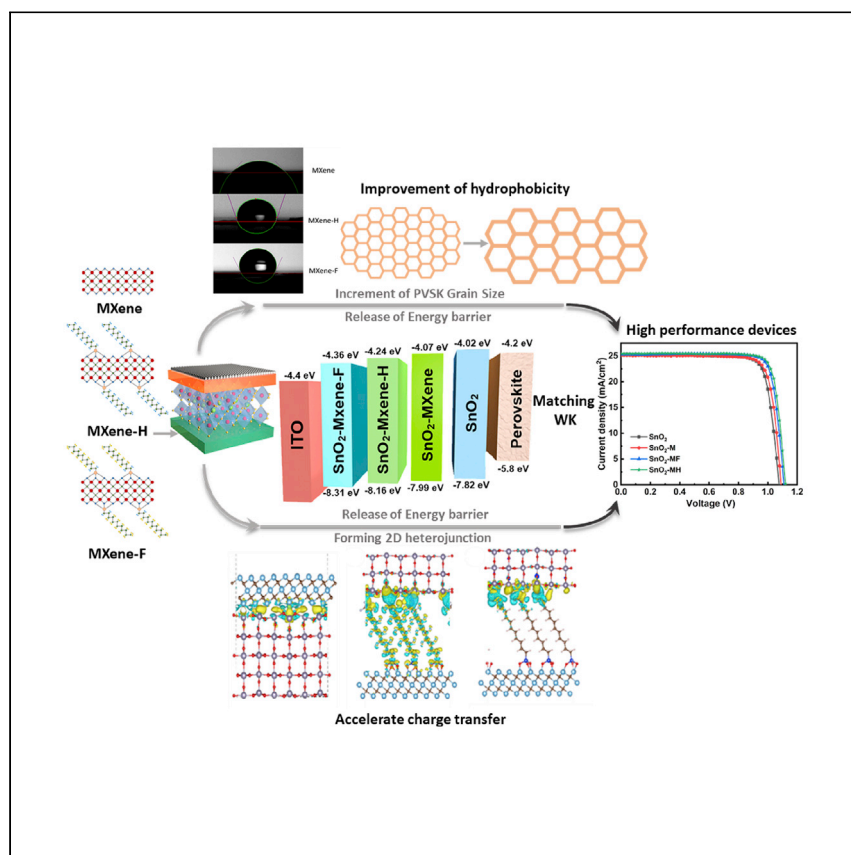


Article

# Functionalized-MXene-nanosheet-doped tin oxide enhances the electrical properties in perovskite solar cells



Li Yin, Chenguang Liu,  
Changzeng Ding, ..., Li Yang,  
Chang-Qi Ma, Cezhou Zhao

chun.zhao@xjtlu.edu.cn (C.Z.)  
cqma2011@sinano.ac.cn (C.-Q.M.)

Highlights

Functionalized MXene adjusts work function and surface energy of SnO<sub>2</sub> to increase  $V_{oc}$

Functionalized MXene dopants passivate the defects and accelerate the charge transfer

The device based on SnO<sub>2</sub>-MH ETL shows excellent PCE and stability

**Q11** Yin et al. report functionalized-MXene-enhanced SnO<sub>2</sub> as an ETL for perovskite solar cells with efficiency up to 24.12%. Functionalized MXene dopants improve energy-band alignment, reduce macroscopic defects, and ameliorate recombination in the interface between the active layer and the SnO<sub>2</sub> ETL. Hence, optimized devices show high FFs and PCEs with excellent moisture resistance and light operation stability.



## Article

## Functionalized-MXene-nanosheet-doped tin oxide enhances the electrical properties in perovskite solar cells

Li Yin,<sup>1,5</sup> Chenguang Liu,<sup>4</sup> Changzeng Ding,<sup>2,3</sup> Chun Zhao,<sup>1,5,7,\*</sup> Ivona Z. Mitrovic,<sup>5</sup> Eng Gee Lim,<sup>1</sup> Haibin Wang,<sup>1</sup> Yi Sun,<sup>1,5</sup> Yunfei Han,<sup>2,3</sup> Zerui Li,<sup>2,3</sup> Li Yang,<sup>6</sup> Chang-Qi Ma,<sup>2,3,\*</sup> and Cezhou Zhao<sup>1</sup>

## SUMMARY

An appropriate electron transport layer (ETL) with better energy alignment and enhanced charge transfer, thereby helping efficient extraction and transport of photogenerated carriers, is essential to achieve the creation of high-performance devices. In this work, we use functionalized MXene modified with fluoroalkylsilane and dodecyltrimethoxysilane molecules, denoted as SnO<sub>2</sub>-MF and SnO<sub>2</sub>-MH, as nanosheet dopants in the SnO<sub>2</sub> ETL. From density functional theory (DFT) calculations and ultraviolet photoelectron spectra (UPS) spectra, we see that better band alignment is achieved for the SnO<sub>2</sub>-MH ETL. Meanwhile, functionalized MXene nanosheets represent high electrical conductivity and mobility and could form zero Schottky barrier heterojunction with SnO<sub>2</sub>, effectively and rapidly enhancing carrier transfer. Finally, the suitable surface energy achieved by functionalized MXene additives can enlarge the grain size of perovskite thin films. Consequently, a significant improvement of power conversion efficiency (PCE) from 20.98% to 23.66% (24.12% for the champion device with a fill factor [FF] over 0.84) can be achieved for devices based on the SnO<sub>2</sub>-MH ETL, which also possess improved moisture resistance and operational stability.

## INTRODUCTION

There has been enormous interest in hybrid organic-inorganic perovskite solar cells (PSCs) for their superior properties, including tuned band gap, low-cost solution processing, high mobility, long charge-diffusion length, and high tolerance to defects.<sup>1–5</sup> In the last decade, the power conversion efficiency (PCE) of PSCs has significantly improved from 3.8% to 25.5%.<sup>4,6</sup> For PSCs, an exquisite and suitable electron transport layer (ETL) is crucial to achieving a high PCE and robust stability, including alignment of energy level with perovskite materials and high electron mobility leading to satisfied V<sub>OC</sub> and excellent ability to extract carriers.<sup>7–9</sup> Since it has demonstrated a suitable energy level relative to the active layer and excellent optical properties,<sup>10,11</sup> SnO<sub>2</sub> is widely used as the ETL in n-i-p planar solar cells. There are various methods for deposition, such as chemical-bath deposition, sputtering, e-beam evaporation, atomic-layer deposition, and nanoparticle-solution deposition, among which nanoparticle-solution deposition is extensively considered for its lower temperature solution fabrication compatibility.<sup>12–16</sup> However, the conductivity of SnO<sub>2</sub> is lower than TiO<sub>2</sub>.<sup>11</sup> Moreover, nanoparticle-based PSCs have higher V<sub>OC</sub> deficits than those using TiO<sub>2</sub> as the ETL.<sup>17</sup> Hence, numerous proposed passivation methods have been extensively investigated for both bulks of SnO<sub>2</sub> and the interface

<sup>1</sup>School of Science, School of Advanced Technology, Xi'an Jiaotong-Liverpool University, Renai Road, Suzhou 215123, China

<sup>2</sup>School of Nano-Tech and Nano-Bionics, University of Science and Technology of China, 398 Jinzhai Road, Hefei 230026, China

<sup>3</sup>i-lab, Suzhou Institute of Nano-Tec and Nano-Bionics, Chinese Academy of Sciences (CAS), 398 Ruoshui Road, SEID, SIP, Suzhou 215123, China

<sup>4</sup>School of Robotics, Xi'an Jiaotong-Liverpool University, Renai Road, Suzhou 215123, China

<sup>5</sup>Department of Electrical Engineering and Electronics, University of Liverpool, Liverpool L69 3GJ, UK

<sup>6</sup>Department of Chemistry, Xi'an Jiaotong-Liverpool University, Renai Road, Suzhou 215123, China

<sup>7</sup>Lead contact

\*Correspondence: [chun.zhao@xjtlu.edu.cn](mailto:chun.zhao@xjtlu.edu.cn) (C.Z.), [cqma2011@sinano.ac.cn](mailto:cqma2011@sinano.ac.cn) (C.-Q.M.)  
<https://doi.org/10.1016/j.xcrp.2022.100905>



between the SnO<sub>2</sub> layer and active layer, such as ionic-compounds doping,<sup>18–20</sup> acids treatment,<sup>14,21</sup> self-assembled molecule (SAM) insertion,<sup>22,23</sup> and bilayer ETL formation,<sup>24–26</sup> to enable a graded band alignment, ameliorate surface-wetting property, improve conductivity, and reduce recombination center.<sup>20,23,27,28</sup>

MXenes, known as M<sub>n+1</sub>X<sub>n</sub>T<sub>x</sub>, is a new family of two-dimensional (2D) materials firstly found in 2011, where M is an early transition metal, X represents C or/and N, and T<sub>x</sub> means the surface terminations.<sup>29,30</sup> So far, the reported MXenes include Ti<sub>3</sub>C<sub>2</sub>T<sub>x</sub>, Ti<sub>2</sub>CT<sub>x</sub>, Nb<sub>2</sub>CT<sub>x</sub>, V<sub>3</sub>CT<sub>x</sub>, Ti<sub>3</sub>CNT<sub>x</sub>, Ta<sub>4</sub>C<sub>3</sub>T<sub>x</sub>, Nb<sub>4</sub>C<sub>3</sub>T<sub>x</sub>, etc.<sup>29,31–33</sup> Ti<sub>3</sub>C<sub>2</sub>T<sub>x</sub> is widely used in PSCs for its high electrical conductivity as well as mobility,<sup>34</sup> including as an additive for both the active layer (AL)<sup>35,36</sup> and the ETL,<sup>37–43</sup> as the ETL/hole-transport layer (HTL),<sup>44–48</sup> or as the bilayer ETL/HTL,<sup>49</sup> and it can be deposited as an electrode.<sup>50</sup> In recent years, functionalized MXene materials with different terminate chemical groups have been well developed to further adjust the surface potential,<sup>51</sup> hydrophilicity,<sup>52,53</sup> or work function.<sup>54</sup> The optimization of these properties, including hydrophilicity and work function, has been sufficiently proved to enhance the performance of PSCs through increasing perovskite grain size or eliminating potential barriers.<sup>37,39</sup> The reported MXene used in PSCs and their function with related parameters are summarized in Table S1 in detail. However, a comprehensive investigation of the significant PCS performance enhancement by functionalized MXene materials is lacking in reports from recent literatures.

Herein, we demonstrate two surface-functionalization strategies for Ti<sub>3</sub>C<sub>2</sub>T<sub>x</sub> with dodecyltrimethoxysilane and fluoroalkylsilane (FOTS) molecules to form a self-assembled monolayer on the MXene, denoted as MXene-H and MXene-F, respectively. The proposed surface-functionalization strategy for Ti<sub>3</sub>C<sub>2</sub>T<sub>x</sub> is initiated elaborately to modify SnO<sub>2</sub> thin films, thereby improving energy band alignment, reducing macroscopic defects, and ameliorating the recombination in the interface between the AL and the SnO<sub>2</sub> ETL. Moreover, the crystal size of the perovskite is also enlarged through the proposed strategy toward regulating suitable surface energy via MXene-F and MXene-H. Through density functional theory (DFT) calculation and ultraviolet photoelectron spectra (UPS) tests, it can be found that MXene-H-doped SnO<sub>2</sub> shows better band alignment with the AL. Moreover, by forming nanoscale heterojunctions, zero Schottky barriers can be achieved accordingly, which is beneficial for the transportation of electrons. Finally, suitable surface energy could be achieved by adding functionalized MXene dopants, indicating a larger grain size and a higher V<sub>OC</sub>. For the MXene-H-doped ETL devices, the related PCE significantly increased from 20.98% to 23.66% (24.12% for the champion device with a fill factor [FF] over 0.84) compared with the undoped ETL device with the FAPbI<sub>3</sub> system. Furthermore, both optimal devices show higher moisture-resistance stability and operation stability.

## RESULTS AND DISCUSSION

### Properties of functionalized MXene

The device with an ITO/SnO<sub>2</sub>/perovskite/Spiro-OMeTAD/MoO<sub>3</sub>/Ag planar structure and functionalized MXene structure is shown in Figure 1 and Figure S1. The water contact angle is shown in Figure S2 and suggests that the two types of SAM modifications change the wettability of MXene nanosheets. The original MXene film with a water contact angle (θ) of 42.1° is much lower than that of MXene-H and MXene-F, which show 106.7° and 114.9°, respectively, indicating that the trimethoxy silane group of FOTS and dodecyltrimethoxysilane connects with the hydroxyl group in the surface of MXene, causing a decrease in surface energy.

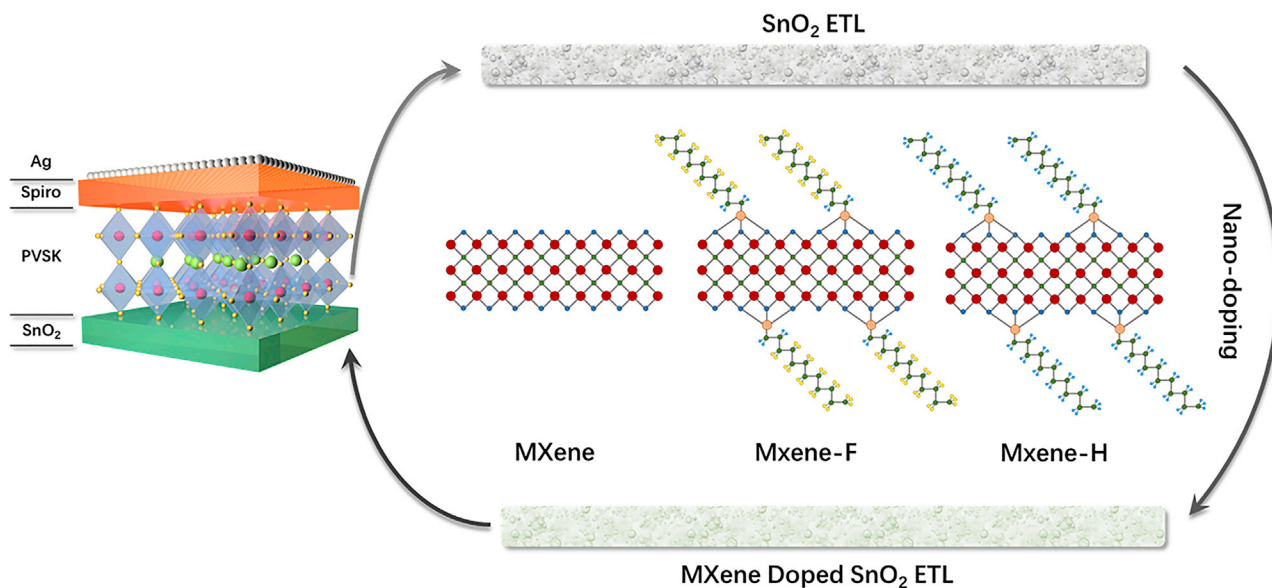


**Figure 1. Structural schematic**

Device structure and crystal structures of MXene, MXene-F, and MXene-H.

To investigate the functionalized MXene materials, X-ray photoelectron spectroscopy (XPS) has been used to explore its chemical changes. Figures 2D, S3, and S4 show the XPS spectra of revealing chemical compositions, including Ti 2p, C 1s, O 1s, F 1s, and Si 2p spectra of MXene and MXene-F as well as MXene-H. The Ti 2p<sub>1/2</sub> spectrum reveals five concomitant peaks at 461, 461.5, 462.9, 464.2, and 466.2 eV,<sup>55,56</sup> corresponding to Ti–C, Ti<sup>2+</sup>, Ti<sup>3+</sup>, and Ti–O as well as C–Ti–F<sub>x</sub>, and it also has an area ratio of 1:2 compared with the 2p<sub>3/2</sub> spectrum. For C 1s spectra, two characteristic peaks of MXene-F appear at 291.0 and 293.2 eV (Figure 2F), indicating –CF<sub>2</sub> and –CF<sub>3</sub> contributed by FOTS,<sup>53</sup> which proves that the FOTS molecules were provided by large fluorine-containing functional groups on the surface of MXene. Moreover, another piece of evidence could attest to this verdict for in F 1s spectra of MXene-F, as the C–F species from FOTS can also be detected at 688.2 eV (Figure 2F).<sup>57</sup> Finally, for both MXene-F and MXene-H, the Si–O could be seen in O 1s spectra (Figures 2E and 2I) at 532.9 eV and in the Si 2p spectra (Figures 2H and 2L) at 102.4 eV.<sup>53</sup> This indicates that the highly stable Si–O–MXene bonds are formed by organosilanes condensed in FOTS and dodecyltrimethoxysilane and –OH on the surface of MXene,<sup>23</sup> which has also been proved in  $\theta$  measurements.

#### The role of functionalized MXene nanosheet dopant

Figure 3 shows the XPS spectra of SnO<sub>2</sub> and SnO<sub>2</sub> with different MXene samples. There is an apparent primary peak for MXene-doped SnO<sub>2</sub>, MXene-F-doped SnO<sub>2</sub>, and MXene-H-doped SnO<sub>2</sub>, denoted as SnO<sub>2</sub>-M, SnO<sub>2</sub>-MF, and SnO<sub>2</sub>-MH, respectively, found at 529.7 eV, representing the Ti–O bond. It could be caused by partial oxidation in the synthesis process<sup>58</sup> and the annealing process of MXene-doped SnO<sub>2</sub> film during the fabrication of the devices. Furthermore, the fewer Ti-based oxides in the film are considered to be beneficial in forming a semiconductor oxide heterojunction.<sup>37</sup>

Meanwhile, the Si–O could also be detected in O 1s spectra at 532.9 eV, indicating that Si–O–MXene bonds exist in the SnO<sub>2</sub>-MF and SnO<sub>2</sub>-MH films. Moreover, other peaks

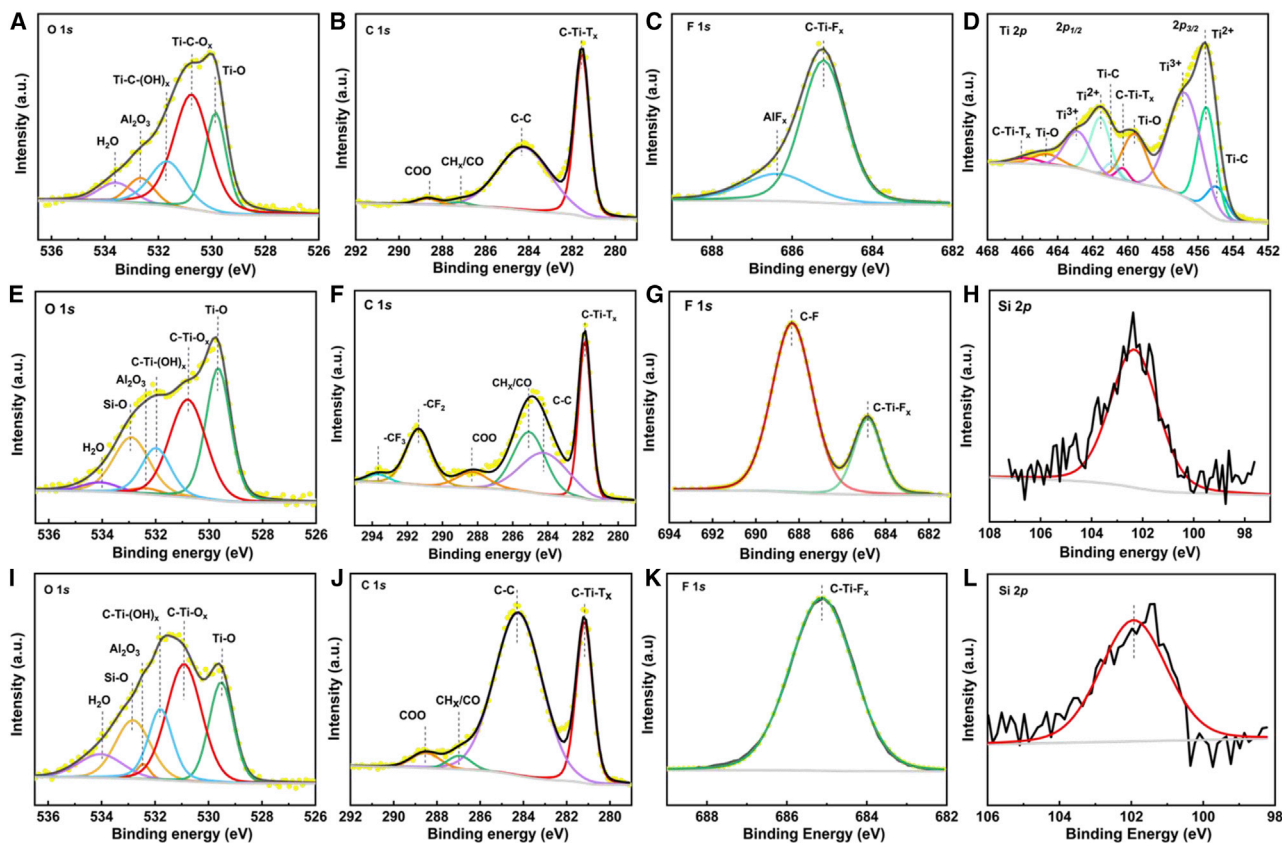


**Figure 2.** XPS spectra of  $\text{SnO}_2$  and  $\text{SnO}_2$  with different MXene samples

(A–D) O 1s, C 1s, F 1s, and Ti 2p spectra of MXene.

(E–H) O 1s, C 1s, F 1s, and Si 2p spectra of MXene-F.

(I–L) O 1s, C 1s, F 1s, and Si 2p spectra of MXene-H.

have binding energies at 530.2, 530.8, and 531.8 eV attributed to Sn-O, hydroxyl group, adsorbed oxygen, and H-O-H.<sup>59</sup> It is worth mentioning that -OH groups could result in traps during the  $\text{SnO}_2$  film-fabrication process, degrading the device's performance.<sup>60</sup> As shown in Figures 3B and 3C, it can be seen that the hydroxyl group's peak at 530.8 eV dramatically decreased due to FOTS as well as dodecyltrimethoxysilane, which suggests that the hydroxyl groups are eliminated. Moreover, in Figure S5, the Sn  $3d_{3/2}$  and Sn  $3d_{5/2}$  orbitals could be found at 495.1 and 486.6 eV, demonstrating that the Sn atoms are in the form of  $\text{SnO}_2$  without any alterations.

Atomic force microscopy (AFM) images of the films of  $\text{SnO}_2$  are illustrated in Figure S6. For  $\text{SnO}_2$ -M,  $\text{SnO}_2$ -MF, and  $\text{SnO}_2$ -MH, some "light spots" indicate the random distribution of MXene nanosheets, which can also be observed in the top-view scanning electron microscopy (SEM) in Figure S7. The root mean square (RMS) roughnesses of  $\text{SnO}_2$ ,  $\text{SnO}_2$ -M,  $\text{SnO}_2$ -MF, and  $\text{SnO}_2$ -MH are 3.77, 4.23, 4.28, and 3.97 nm, respectively, demonstrating a negligible influence with MXene nanosheet doping. Moreover, as mentioned above, the  $\theta$  is increased with the two functional groups. After a thermal-annealing process, the perovskite film could not completely cover the substrate, resulting in pinholes on the film for a superhydrophobic substrate. Since the Gibbs free energy for the formation of a crystal nucleus can be calculated as Equation (1), a smaller  $\theta$  leads to lower Gibbs free energy, which is beneficial for nucleation.<sup>61</sup>

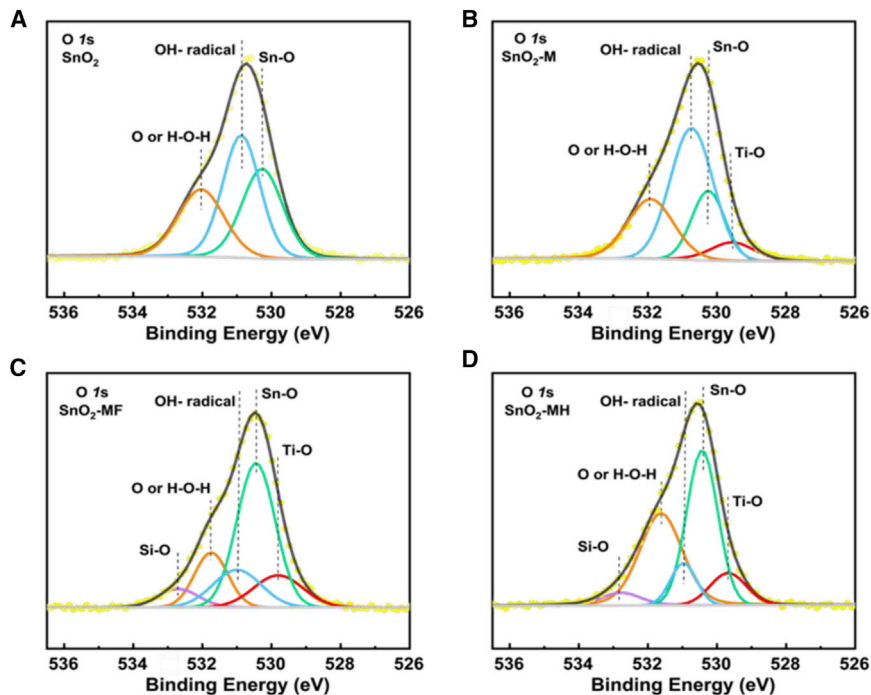


**Figure 3.** XPS spectra of O 1s of SnO<sub>2</sub> and SnO<sub>2</sub> with different MXene samples

- (A) SnO<sub>2</sub>.
- (B) SnO<sub>2</sub>-M.
- (C) SnO<sub>2</sub>-MF.
- (D) SnO<sub>2</sub>-MH.

$$\Delta G_{\text{hetero}} = \frac{(2 + \cos \theta)(1 - \cos \theta)^2}{4} \cdot \Delta G_{\text{homo}} \quad (\text{Equation 1})$$

However, if the substrate becomes very hydrophilic, even if the film uniformity increases, the grain size would become smaller due to the high density of nuclei. Hence, the ETL must balance hydrophilicity and hydrophobicity to form a uniform film with a large grain size.<sup>61,62</sup> Figure S8 demonstrates the  $\theta$  of SnO<sub>2</sub>, SnO<sub>2</sub>-M, SnO<sub>2</sub>-MH, and SnO<sub>2</sub>-MF at 5.8°, 10.4°, 15.0°, and 17.2°, indicating the suitable surface energy to perovskite film formation. Another piece of evidence for this hypothesis is the larger grain size for the perovskite films of SnO<sub>2</sub>-MF and SnO<sub>2</sub>-MH ETLs. Figures 4A–4C shows the morphology of a perovskite deposited on these three types of ETLs. All films are uniform without any pinhole for the slight  $\theta$ . Although, the perovskite average grain size of SnO<sub>2</sub>-MF and SnO<sub>2</sub>-MH only increased to more than 650 nm, as shown in the box chart in Figure 4D. However, from AFM images of different perovskite films (Figure S9), the perovskite deposited on SnO<sub>2</sub>-MF as well as SnO<sub>2</sub>-MH ETLs shows a higher RMS value, representing a larger grain size; the larger grain size could ultimately result in a higher  $V_{\text{OC}}$ .

The cross-sectional SEM image of the device is shown in Figure 5A: indium tin oxide (ITO), MXene-doped SnO<sub>2</sub>, perovskite, Spiro-OMeTAD, and MoO<sub>3</sub>/Ag are shown from the bottom to the top. The thickness of the ETL, the AL, and the HTL are approximately 39.7, 464, and 105 nm, respectively. The short-circuit current density ( $J_{\text{SC}}$ ) has a slight improvement, as shown in the external quantum efficiency (EQE) performance (Figure 4B). The integrated current densities increase from 23.2 to 23.5 mA/cm<sup>2</sup> for the CsFAMAPbI<sub>3</sub> system and from 25.1 to 25.4 mA/cm<sup>2</sup> for the FAPbI<sub>3</sub> system. The high EQE values are potentially due to the better

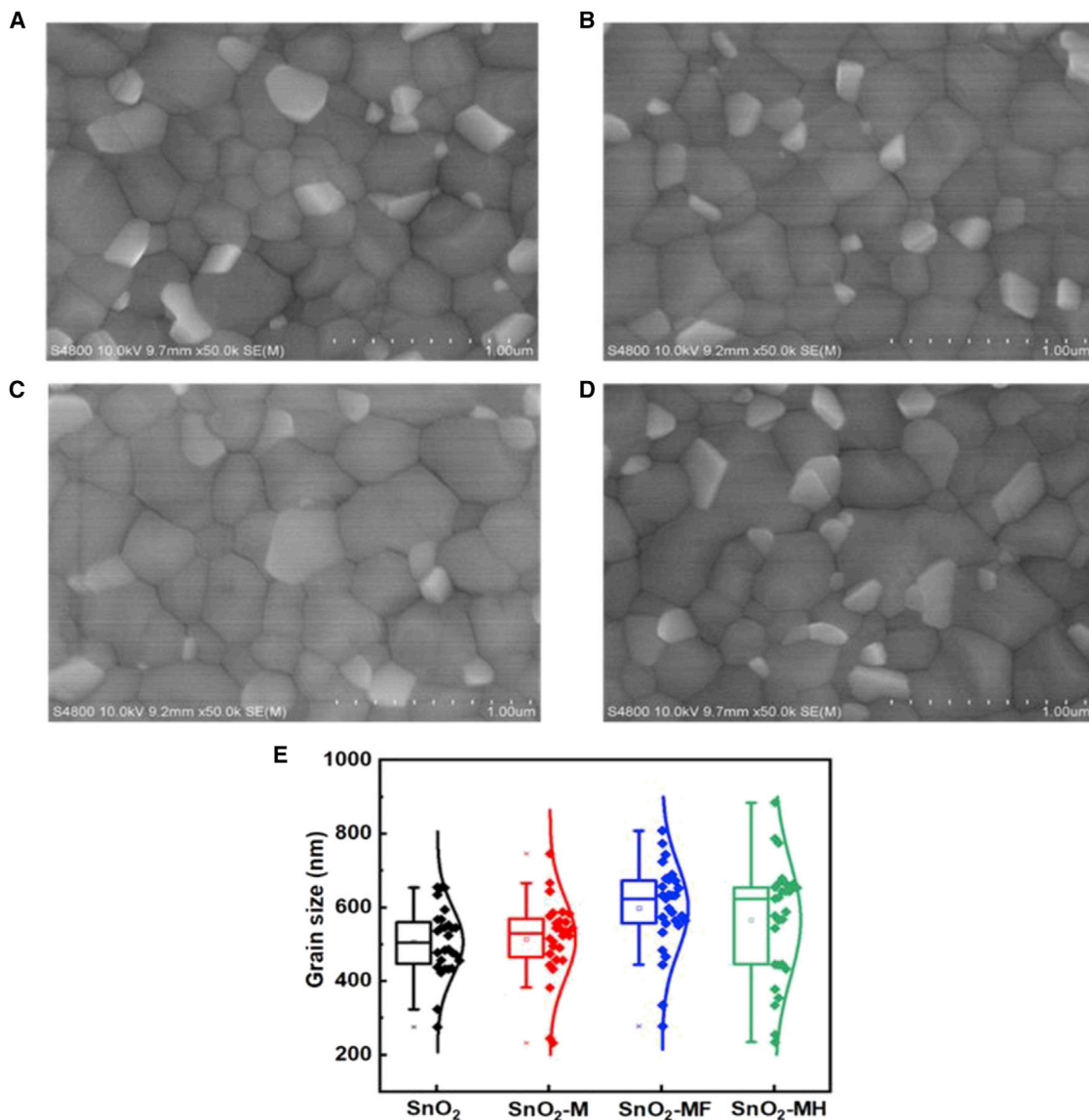


**Figure 4. SEM images of perovskite layers on each ETL with the CsFAMAPbI<sub>3</sub> system**

(A) SnO<sub>2</sub>.

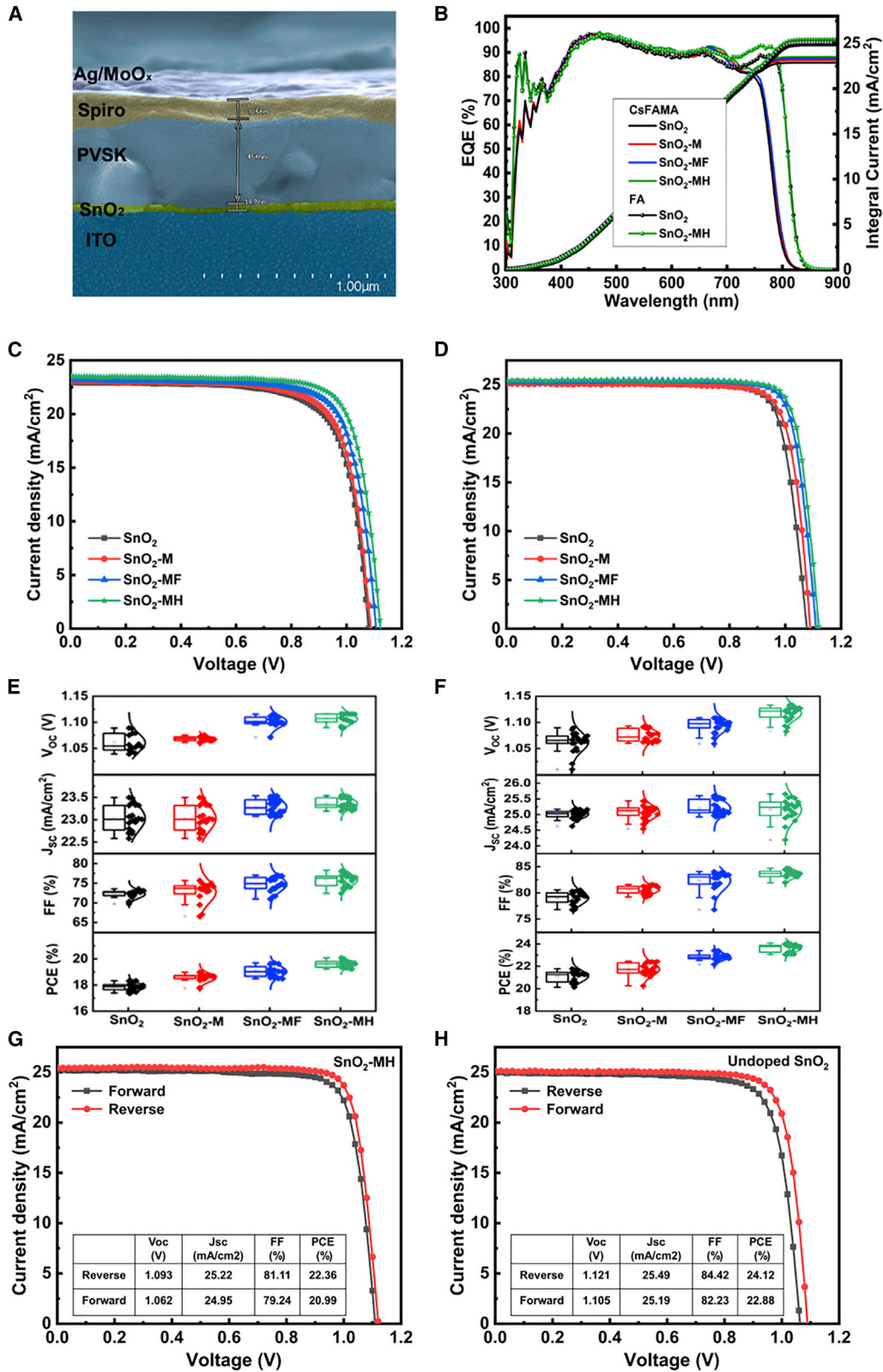
(B) SnO<sub>2</sub>-M.

(C) SnO<sub>2</sub>-MF.

(D) SnO<sub>2</sub>-MH.

(E) Grain-size box chart of the perovskite film with different ETLs.

electron-extraction capability reported in previous works.<sup>63</sup> For the CsFAMAPbI<sub>3</sub> system, the average PCE reaches the best value of 19.33% and 19.76% for SnO<sub>2</sub>-MF and SnO<sub>2</sub>-MH devices, respectively, illustrating a significant improvement compared with that of control devices (17.79%). The champion device of the SnO<sub>2</sub>-MH-doped device achieves 20.26% with negligible hysteresis (Figures 5C and S10). Moreover, for the FAPbI<sub>3</sub> system, the average PCE increased from 20.98% to 22.58% and 23.66% for SnO<sub>2</sub>-MF- and SnO<sub>2</sub>-MH-doped devices (Figure 5D). We achieve a champion PCE of 24.12% with negligible hysteresis (Figure 5H). Particularly worth mentioning is that the FF could achieve 84.42%, and the ideal values of FF could be calculated as follows:



$$FF_0 = \frac{V_{oc} - \ln(V_{oc} + 0.72)}{V_{oc} + 1} \quad (\text{Equation 2})$$

$$V_{oc} = qV_{oc}/nkT \quad (\text{Equation 3})$$

$n$  and  $k$  represent the ideality factor and Boltzmann's constant, respectively. Hence, from the  $V_{OC}$  versus light-intensity test shown in Figure 6D, the ideality factor  $n$  could be achieved, and the value of  $FF_0$  is 87.14%. Additionally, the band gap of our perovskite materials is 1.5 eV,<sup>64</sup> which can be calculated from EQE data ( $\lambda_g \cong 830$  nm), and the S-Q limit value of FF is 89.9%.<sup>65</sup> This indicates that the nonradiative recombination is strongly reduced by MXene-H dopants. Table 1 summarizes the average device characteristics.

The photovoltaic parameters are shown in Figures 5E and 5F for different AL systems, and all parameters are improved for MXene-doped devices. Functionalized MXene material dopants significantly increase PCE because of the main improvement of  $V_{OC}$  and FF. Furthermore, we also evaluated the effect of additional concentrations, as shown in Figure S11 and Table S2. It can be found that when the doping concentration is 0.03 wt %, the device displays the best performance, and with a higher doping concentration, the performance of the device is degraded accordingly. One potential mechanism for this phenomenon might be that the original MXene cannot extract electrons effectively with the increasing doping concentration due to a lack of Ti-O bond. It is also hard to be oxidized in the annealing process, thereby improving the electron extraction ability of MXene.<sup>46</sup>

However, compared with the performance of SnO<sub>2</sub>-MH ETL devices, SnO<sub>2</sub>-MF ETL devices reveal lower  $V_{OC}$ s and FFs. From the band perspective, we tried to investigate the reason for this phenomenon. The energy level and work function were then probed with UPS and DFT calculations. Figures 6A–6D show the calculation work functions of SnO<sub>2</sub>, SnO<sub>2</sub>-M, SnO<sub>2</sub>-MF, and SnO<sub>2</sub>-MH, which are 3.78, 3.67, 4.02, and 4.32 eV. Meanwhile, the work function has an enormous variation for the original MXene, MXene-H, and MXene-F (Figures S12 and S13).

To understand why the doping could change the work function, we further evaluated the first principles of optimized structures and electron-density differences (Figure S14). The yellow and green parts represent charge accumulation and depletion, respectively. The charge-depletion areas of SnO<sub>2</sub>-MH and SnO<sub>2</sub>-MF are larger than that of SnO<sub>2</sub>-M, and the chain of -CF<sub>2</sub> could also contribute to more charge-depletion areas due to the solid electron-withdrawing effect of the F atom, thereby increasing the work function.<sup>66,67</sup> From UPS spectra (Figure 6E) and  $\tau_{auc}$  plot (Figure S15), the band energy diagram can ultimately be achieved, as shown in Figure 6F. The conduction band (CB) of SnO<sub>2</sub>-MH is lower than that of the CsFAMAPbI<sub>3</sub> perovskite<sup>68</sup> and has less energy band barrier, which is another reason for the uppermost  $V_{OC}$  besides the larger grain size. Moreover, for the FAPbI<sub>3</sub> perovskite, the CB of

#### Figure 5. Photovoltaic performance of perovskite solar cells

- (A) The cross-sectional image with ITO/SnO<sub>2</sub>-MH/perovskite/Spiro/Ag structure.
- (B) EQE spectra of the champion devices based on each ETL.
- (C) J-V curves of the champion devices based on each ETL under reverse scans for CsFAMAPbI<sub>3</sub> system.
- (D) J-V curves of the champion devices based on each ETL under reverse scans for FAPbI<sub>3</sub> system.
- (E) Photovoltaic parameters of solar cells with different ETLs for CsFAMAPbI<sub>3</sub> system.
- (F) Photovoltaic parameters of solar cells with different ETLs for FAPbI<sub>3</sub> system.
- (G) Scan direction-dependent J-V curve of devices for FAPbI<sub>3</sub> PSCs without doping.
- (H) Scan direction-dependent J-V curve of devices for FAPbI<sub>3</sub> PSCs based on SnO<sub>2</sub>-MH ETL.

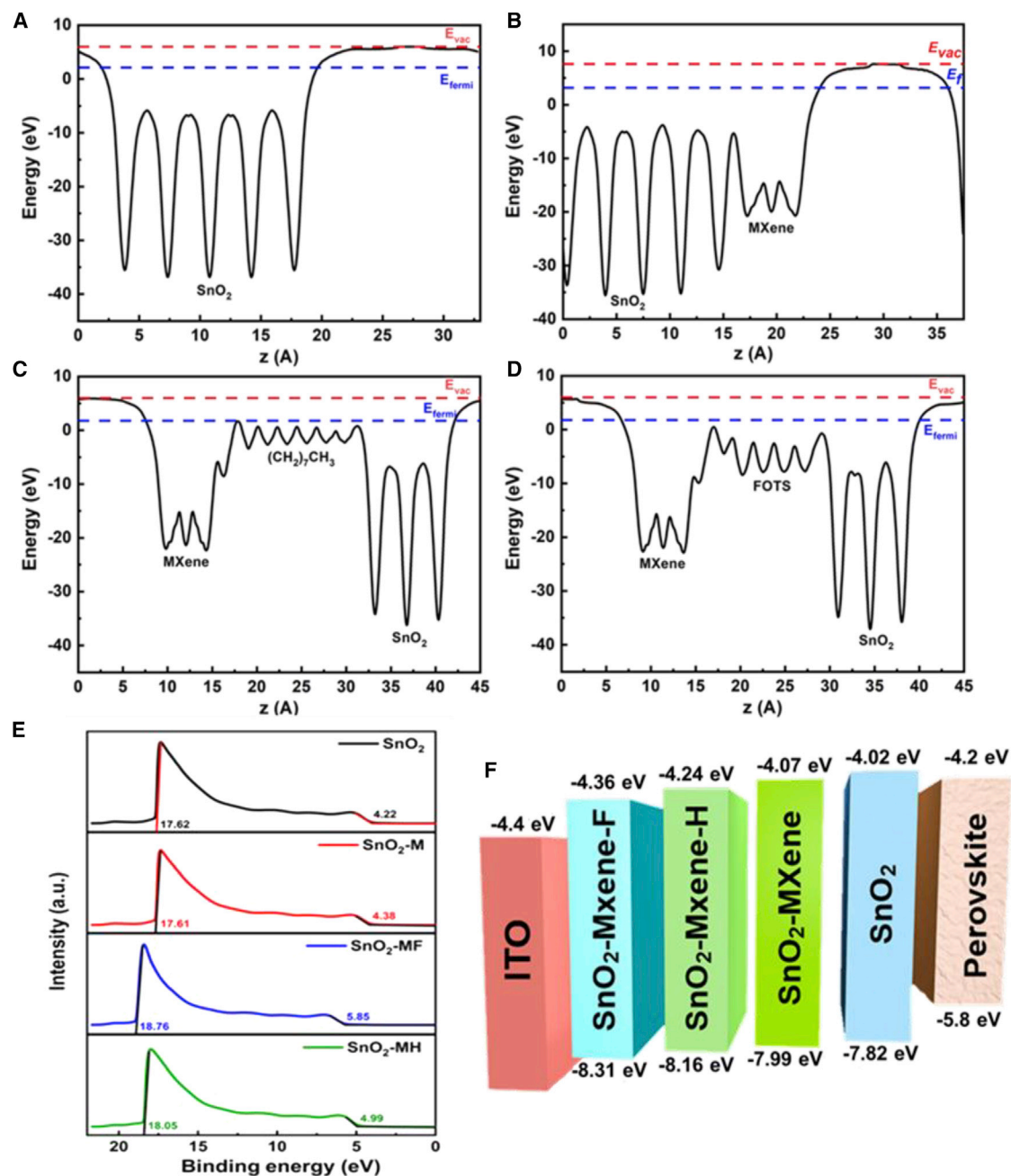


**Figure 6. Band-alignment analysis of different SnO<sub>2</sub> ETLs**

(A–D) DFT calculations for the plane-averaged electrostatic potential of SnO<sub>2</sub>, SnO<sub>2</sub>-M, SnO<sub>2</sub>-MF, and SnO<sub>2</sub>-MH.

(E) UPS spectra of the four types of ETLs.

(F) Energy-level diagram of the ITO/ETL/AL structure based on SnO<sub>2</sub>, SnO<sub>2</sub>-M, SnO<sub>2</sub>-MF, and SnO<sub>2</sub>-MH as the ETLs.

SnO<sub>2</sub>-MH is also suited for FAPbI<sub>3</sub>.<sup>15</sup> Hence, from both DFT calculations and UPS spectra, it can be seen that a better band alignment is achieved for SnO<sub>2</sub>-MH.

Moreover, Huang et al. proved that nanoscale heterojunctions could be formed after adding MXene nanosheets.<sup>39</sup> Hence, the influences of surface functional groups on the Schottky barrier regulation at the heterojunction interface are also investigated by DFT calculations (Figure S16). The height of the Schottky barrier ( $\phi$ ) on

**Table 1. Performance parameters of CsFAMAPbI<sub>3</sub> system and FAPbI<sub>3</sub> system PCSs with MXene-doped SnO<sub>2</sub> as ETLs<sup>a</sup>**

Active layer	ETL	V <sub>oc</sub> (V)	J <sub>sc</sub> (mA/cm <sup>2</sup> )	FF (%)	PCE (%)
CsFAMAPbI <sub>3</sub>	SnO <sub>2</sub>	1.064 ± 0.025	23.09 ± 0.63	71.74 ± 1.92	17.62 ± 0.39
CsFAMAPbI <sub>3</sub>	SnO <sub>2</sub> -M as ETL	1.069 ± 0.022	23.18 ± 0.84	72.83 ± 2.85	18.05 ± 0.72
CsFAMAPbI <sub>3</sub>	SnO <sub>2</sub> -MF as ETL	1.099 ± 0.016	23.22 ± 1.15	74.75 ± 2.29	19.07 ± 0.86
CsFAMAPbI <sub>3</sub>	SnO <sub>2</sub> -MH as ETL	1.106 ± 0.026	23.47 ± 0.45	75.96 ± 2.28	19.71 ± 0.54
FAPbI <sub>3</sub>	SnO <sub>2</sub>	1.062 ± 0.065	25.01 ± 0.47	79.03 ± 1.16	20.98 ± 1.55
FAPbI <sub>3</sub>	SnO <sub>2</sub> -M as ETL	1.075 ± 0.031	25.07 ± 0.78	80.60 ± 0.72	21.72 ± 0.82
FAPbI <sub>3</sub>	SnO <sub>2</sub> -MF as ETL	1.094 ± 0.027	25.21 ± 0.66	81.87 ± 3.21	22.58 ± 2.05
FAPbI <sub>3</sub>	SnO <sub>2</sub> -MH as ETL	1.118 ± 0.037	25.44 ± 0.42	83.18 ± 1.11	23.66 ± 0.48

<sup>a</sup>Calculated from 16 individual devices.

the metal/semiconductor heterojunction is defined as the energy difference between the Fermi level and the band edge:

$$\varphi_n = E_{CB} - E_F, \quad \varphi_p = E_F - E_{VB} \quad (\text{Equation 4})$$

$\varphi_n$  and  $\varphi_p$  indicate the height of the Schottky barrier for *n*- and *p*-types, and  $E_F$ ,  $E_{CB}$ , and  $E_{VB}$  stand for Fermi level, the bottom of CB, and the top of the valence band (VB), respectively. If  $\varphi_n < \varphi_p$ , the metal/semiconductor heterojunction belongs to an *n*-type contact; otherwise, it is a *p*-type contact. When  $\varphi_n$  or  $\varphi_p$  is close to 0 or equal negative value, the interface contact of zero Schottky barriers could be achieved. These two metal/semiconductor heterojunctions show *n*-type contact characteristics with  $\varphi_n = -0.49$  and  $-0.58$  eV. Zero Schottky barrier contact is beneficial for electron transport across the interface,<sup>69</sup> consistent with previous EQE results.

Then, to investigate the recombination kinetics of perovskite films on different ETLs, steady-state photoluminescence (PL) and time-resolved PL (TRPL) are used, as shown in Figures 7A and 7B. It can be seen that a significant PL quench is obtained for the SnO<sub>2</sub>-MH device, again confirming the excellent electron extraction of the device. Moreover, for TRPL, the relevant data are demonstrated in Table S3.  $\tau_1$  correlates with radiative recombination of free charge carriers due to traps, which means the recombination before free charge carriers are extracted by the ETL. There is a negligible difference of  $\tau_1$ . Moreover,  $\tau_2$  of the SnO<sub>2</sub>-MH film shows the least time, indicating that this ETL effectively extracts electrons due to the high mobility of the thin film. Furthermore, to estimate the trap density of bulk, the space-charge-limited current (SCLC) technique is initiated and devoted to electron-only devices (Figure 7C). The trap density  $N_t$  can be calculated as<sup>70</sup>

$$N_t = \frac{2\varepsilon_0\varepsilon V_{TFL}}{eL^2} \quad (\text{Equation 5})$$

where  $e$  is the elementary charge,  $L$  is the thickness of the perovskite film (Figure 5A),  $\varepsilon$  is the relative dielectric constant,<sup>71</sup>  $\varepsilon_0$  is the vacuum permittivity, and  $V_{TFL}$  is the trap-filling limit voltage. Hence, the trap densities of the perovskite films based on SnO<sub>2</sub>, SnO<sub>2</sub>-M, and SnO<sub>2</sub>-MF as well as SnO<sub>2</sub>-MH ETLs are  $3.21 \times 10^{16}$ ,  $1.76 \times 10^{16}$ ,  $1.44 \times 10^{16}$ , and  $9.93 \times 10^{15}$  cm<sup>-3</sup>, respectively. The reduction of trap density can be partially attributed to the low grain boundary of the perovskite film. Moreover, the diode ideality factor is considered to be a good index to check the carrier recombination mechanism in the device, and it can be achieved by<sup>72</sup>

$$V_{oc} = \frac{nkT}{q} \ln(I^0) + C, \quad (\text{Equation 6})$$

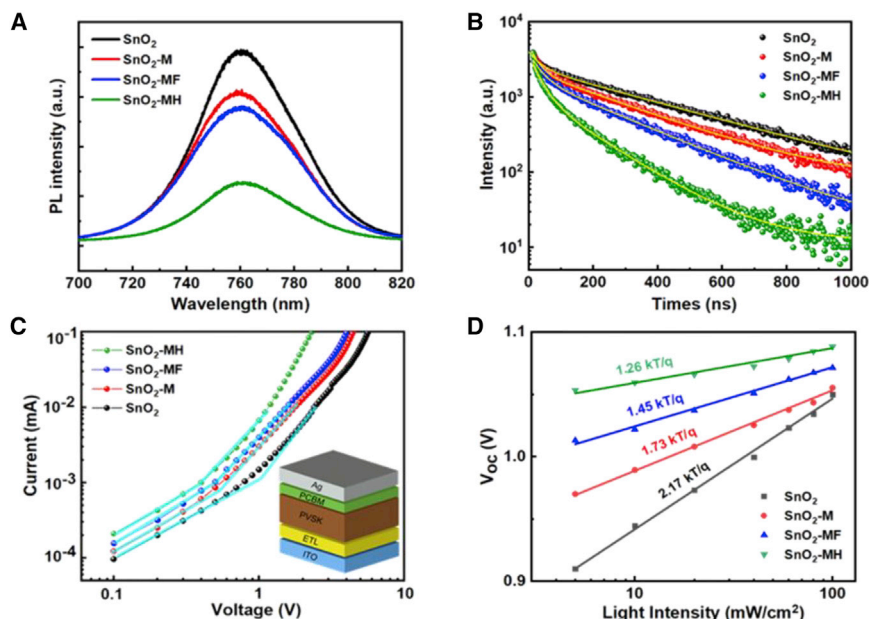


**Figure 7. Charge-recombination kinetics of perovskite films on different SnO<sub>2</sub> ETLs**

(A and B) Steady-state and time-resolved PL (TRPL) spectra of perovskite films on different ETLs. (C) SCLC measurements of electron-only devices based on different ETLs with ITO/ETL/PVSK/PCBM/Ag structure.

(D) VOC versus light intensity.

where  $I$  is light intensity,  $C$  is constant, and  $\alpha$  is the empirical parameter. From Figure 7D, the diode ideality factors of each device based on SnO<sub>2</sub>, SnO<sub>2</sub>-M, SnO<sub>2</sub>-MF, and SnO<sub>2</sub>-MH ETLs can be achieved, which are 2.17, 1.73, 1.45, and 1.26. For the device based on SnO<sub>2</sub>, the ideal factor of more than two indicates that both Shockley-Read Hall (SRH) recombination and interface recombination are essential in this device. The ideal factor for the device based on SnO<sub>2</sub>-MH decreased to 1.26, indicating that trap-assisted recombination is eliminated and band alignment is achieved. This phenomenon also can be proved by electrochemical impedance spectroscopy (EIS) analysis (Figure S17) for the falling  $R_{tr}$  (indicating better electron extraction) and increased  $R_{rec}$  (effectively resisting charge recombination) of the device based on SnO<sub>2</sub>-MH ETLs, which showed the best performance. All devices used in Figure 7 are from the CsMAFAPbI<sub>3</sub> system.

### Stability studies

Finally, the stability issue has been checked for these four devices based on SnO<sub>2</sub>, SnO<sub>2</sub>-M, SnO<sub>2</sub>-MF, and SnO<sub>2</sub>-MH (Figure 8). The devices based on SnO<sub>2</sub>-MF and SnO<sub>2</sub>-MH could maintain almost 80% of initial PCE without any encapsulation after 720 h under 25°C and 30% humidity conditions, contributing to high-quality perovskite films. However, the devices without MXene dopants degraded to less than 60% of the initial PCE simultaneously. Additionally, the reason that the stability of the device based on SnO<sub>2</sub>-MF shows an uptrend after 300 h could be that the better surface energy of the device based on SnO<sub>2</sub>-MF (Figure S8) leads to a higher-quality perovskite film, thereby improving moisture stability. For light stability, it is clear that after 1,000 h of illumination, the device based on SnO<sub>2</sub>-MH as the ETL maintains almost 80% of its initial efficiency, while for the same test duration, the control-group device maintains only 38% relative to its initial efficiency. It is worth mentioning that there is an evident phenomenon that the device recovered after 400 h continual operation.

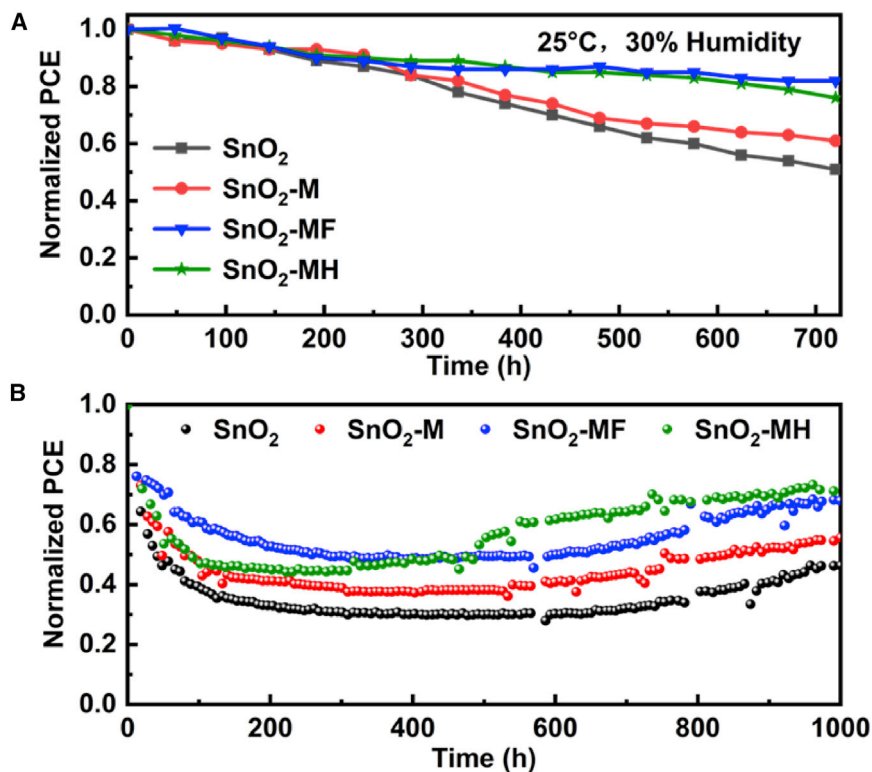


**Figure 8. Stability parameters of devices based on SnO<sub>2</sub>, SnO<sub>2</sub>-M, SnO<sub>2</sub>-MF, and SnO<sub>2</sub>-MH ETLs**  
(A) Without encapsulation under 25°C and 30% humidity ambient atmosphere.  
(B) Operational stability of PSCs over 1,000 h.

The main reason for this phenomenon might be that excessive PbI<sub>2</sub> in the perovskite film disintegrates to metallic Pb and I<sub>2</sub> under light illumination, and thus the generated metallic Pb acts as a quencher for carriers, gradually making the PCEs lower.<sup>73</sup> Moreover, with the operation time increasing, the excessive MA<sup>+</sup> and PbI<sub>2</sub> also form new perovskite film over the initial film as a passivation layer under a small bias voltage (1.2 V operation voltage).<sup>74</sup> This could be why the FF and PCE could recover after a more extended operation.

In summary, we have demonstrated the addition of two types of surface functionalization Ti<sub>3</sub>C<sub>2</sub>T<sub>x</sub> with dodecyltrimethoxysilane and FOTS molecules in a SnO<sub>2</sub>-based ETL, thereby improving energy band alignment, reducing macroscopic defects, and ameliorating the recombination in the interface between the AL and the SnO<sub>2</sub> ETL. Moreover, for two typical perovskite recipes, CsFAMAPbI<sub>3</sub>Br and FAPbI<sub>3</sub>, both devices with modified ETLs show better performance. This work provides a promising potential direction toward achieving high-quality SnO<sub>2</sub> ETLs, and we believe that the desired modifications to the dopant could further enhance the device performance preferably.

## EXPERIMENTAL PROCEDURES

### Resource availability

#### Lead contact

Further information and requests should be directed to and fulfilled by the lead contact, Chun Zhao ([Chun.Zhao@xjtlu.edu.cn](mailto:Chun.Zhao@xjtlu.edu.cn)).

#### Materials availability

This study did not generate new unique materials.

#### Data and code availability

All of the data supporting the results are presented in the main text and [supplemental information](#). Further information and requests for additional data should be directed to the [lead contact](#).

#### Materials

PbI<sub>2</sub>, PbBr<sub>2</sub>, CsI, formamidinium iodide (FAI), methylammonium bromide (MABr), lithium bis(trifluoromethanesulfonyl)imide (LiTFSI), pyridine,4-(1,1-dimethylethyl)-(t-BP), and spiro-OMeTAD were purchased from Xi'an Polymer Light Technology, and dimethylformamide (DMF; purity >99%), dimethyl sulfoxide (DMSO; purity >99%), ethyl acetate (EA; purity >99%), and chlorobenzene (CB; purity >99%) were purchased from J&K Scientific. The SnO<sub>2</sub> colloid solution was purchased from Alfa Aesar (tin (IV) oxide, 15 wt % in water). LiF was purchased from Aladdin (99.9%). HCl was purchased from Sinopharm Chemical Reagent (AR, 36%–38%). MAX Ti<sub>3</sub>AlC<sub>2</sub> was purchased from Jiling 11 Technology (diameter <32 μm).

#### Synthesis of Ti<sub>3</sub>C<sub>2</sub>T<sub>x</sub>

LiF/HCl was employed to etch precursor Ti<sub>3</sub>AlC<sub>2</sub> to synthesize the MXene (Ti<sub>3</sub>C<sub>2</sub>T<sub>x</sub>), as reported previously.<sup>75</sup> Typically, HCl (60 mL, 9 M) and LiF (3 g) were mixed by stirring in a Teflon beaker. Then, the MAX powder was slowly dropped into the etching solution and stirred for 24 h at 40°C. After this reaction, the resultant was washed with de-ionized (DI) water for several centrifugation-rinsing cycles (4,500 RPM for 10 min) until the pH of the solution approached 6. The washed resultant was mixed in 60 mL ethanol during the exfoliation process and kept under ultrasonic for 1.5 h. To get the final dark gray MXene nanosheet, the exfoliated resultant was freeze dried for 48 h.

#### Functionalization of MXene

To get the functionalization of the MXene nanosheet, the freeze-dried MXene nanosheet (200 mg) was dispersed in the precursors (10 wt % in 20 mL ethanol) of dodecyltrimethoxysilane and FOTS for stirring for 24 h, denoted as MXene-H and MXene-F, respectively. After this reaction, the resultant was washed with DI water and ethanol for several centrifugation-rinsing cycles (6,000 RPM for 10 min). The final functionalized MXene nanosheet was collected by freeze drying for 24 h.

#### Instruments and characterization

The current density-voltage (J-V) characters of solar cells were measured with a Keithley 2400 source meter in an N<sub>2</sub> glovebox under a simulated sun AM 1.5 G (Newport VeraSol-2 LED Class AAA Solar Simulator). The EQE of each cell was measured using a home-made incident photon-to-current conversion efficiency (IPCE) system consisting of a 150 W tungsten halogen lamp (Osram64642), a monochromator (Zolix, Omni-I300), an optical chopper, and a current to voltage (I-V) converter (QE-IV Converter, Suzhou D&R Instruments) equipped with lock-in amplifier (Stanford Research Systems SR 830). To simulate the device under 1 sun conditions better, bias light from a 532 nm solid-state laser was introduced to the cell simultaneously. A calibrated Si solar cell was used as a reference. SEM images were gained by a field-emission scanning electron microscope (S-4800) under an accelerating voltage of 10 kV. The AFM images of the films of SnO<sub>2</sub> were studied using a Veeco Dimension 3100 instrument at the ambient temperature in tapping mode. The XPS and UPS measurements were conducted with a PHI 5000 Versaprobe system. The electrochemical impedance spectra were measured using an Autolab electrochemical workstation (Autolab PGSTAT 302 N, Metrohm Autolab B.V.)

The absorption curves of the sample were analyzed by UV-visible spectrometer (Lambda 750, PerkinElmer). PL and TRPL of solar cells were tested by a homemade defects imaging system (LBIC). Operational stability of the cells was performed on a multi-channel solar cell performance decay-testing system (PVLT-G8001 M, Suzhou D&R Instruments) inside an N<sub>2</sub>-filled glovebox (H<sub>2</sub>O < 10 ppm, O<sub>2</sub> < 10 ppm), and the cells were illuminated with a white LED light (D&R Light, L-W5300KA-150, Suzhou D&R Instruments) at a simulated one sun intensity (the initial short current equals the J<sub>SC</sub> measured under standard conditions). The cell's performance was measured by I-V sweeping from 1.2 to −0.05 V, with a step of 0.01 V. The temperature was measured from time to time and was around 40°C–50°C.

### Preparation of the solution

The SnO<sub>2</sub> colloid solution (15 wt %) was diluted to a concentration of 3 wt % by DI water. The solution was ultrasound for 10 min. The K<sub>0.05</sub>Cs<sub>0.05</sub>(FA<sub>0.85</sub>MA<sub>0.15</sub>)<sub>0.95</sub>Pb(l<sub>0.85</sub>Br<sub>0.15</sub>)<sub>3</sub> precursor solution was prepared as reported in our previous work.<sup>76</sup> The FAPbI<sub>3</sub> precursor solution was prepared by dissolving 1.5 mmol PbI<sub>2</sub> and FAI and 35 mol % MAcl in a mixture solvent of DMF/DMSO (1 mL, 4:1 v/v) and being stirred for 1–2 h at room temperature. The OAI solution was prepared by dissolving 5 mg OAI into 1 mL IPA. The spiro-OMeTAD solution was prepared by dissolving 72.3 mg spiro-OMeTAD into 1 mL CB, followed by 17.5 μL Li-TFSI (520 mg/mL in acetonitrile) and 29 μL t-BP. Both OAI and spiro-OMeTAD were stirred overnight at room temperature in the glovebox.

### Solar cell fabrication

ITO glass was cleaned by ultrasonic cleaning through detergent, DI water, acetone, and isopropanol for 30 min. Before use, the ITO substrate was cleaned with UV Ozone for 30 min. Then, the substrate was spin coated with a thin layer of SnO<sub>2</sub> nanoparticles from the SnO<sub>2</sub> colloid solution at 4,000 RPM for 30 s with an accelerated speed of 2,000 RPM. Then, the substrate was annealed in ambient air at 150°C for 30 min.

For the K<sub>0.05</sub>Cs<sub>0.05</sub>(FA<sub>0.85</sub>MA<sub>0.15</sub>)<sub>0.95</sub>Pb(l<sub>0.85</sub>Br<sub>0.15</sub>)<sub>3</sub> AL, the spin-coated process of the perovskite solution was divided into a consecutive two-step process: the spin rate of the first step was 1,000 RPM for 10 s with an accelerated speed of 500 RPM, and the spin rate of the second step was 5,000 RPM for 20 s with accelerated speed of 1,000 RPM. During the second step end of 10 s, 400 μL ethyl acetate was drop coated to treat the perovskite films, and then the perovskite films were annealed at 120°C for 30 min in a glovebox. For the FAPbI<sub>3</sub> AL, the spin rate of this step was 5,000 RPM for 30 s with an accelerated speed of 1,000 RPM. During the end of 10–12 s, 300 μL CB was drop coated to treat the perovskite films, and then the perovskite films were annealed at 150°C for 15 min and 100 °C for 15 min. Then, the film was washed with IPA by dropping several drops at 3,000 RPM and then was heated at 100 °C for 1 min.

After cooling to room temperature, the OAI solution was coated on perovskite films at 5,000 RPM for 30 s with an accelerated speed of 5,000 RPM. Then, the spiro-OMeTAD solution was coated at 3,000 RPM for 30 s with an accelerated rate of 3,000 RPM.

Then 8-nm-thick MoO<sub>3</sub> and 80-nm-thick Ag were deposited on the spiro-OMeTAD film by thermal evaporation with 0.3 and 2 Å/s, respectively.

### SUPPLEMENTAL INFORMATION

Supplemental information can be found online at <https://doi.org/10.1016/j.xcrp.2022.100905>.

## ACKNOWLEDGMENTS

This research was funded in part by the Natural Science Foundation of the Jiangsu Higher Education Institutions of China Program (19KJB510059), the Natural Science Foundation of Jiangsu Province of China (BK20180242), the Suzhou Science and Technology Development Planning Project: Key Industrial Technology Innovation (SYG201924), the University Research Development Fund (RDF-17-01-13), and the Key Program Special Fund in XJTLU (KSF-P-02, KSF-T-03, KSF-A-04, KSF-A-05, KSF-A-07, and KSF-A-18). This work was partially supported by the XJTLU AI University Research Centre, the Jiangsu (Provincial) Data Science, and the Cognitive Computational Engineering Research Centre at XJTLU. I.Z.M. acknowledges the British Council UKIERI project no. IND/CONT/G/17-18/18.) The authors would like to acknowledge the Vacuum Interconnected Nanotech Workstation (Nano-X) of SINANO, CAS for the online XPS/UPS characterization on the MXene samples (project no. A2107).

## AUTHOR CONTRIBUTIONS

L. Yin designed the experiment, fabricated the PSCs, analyzed the data, finished DFT calculations, and wrote the original draft. C.L. synthesized MXene and functionalized MXene. C.D. and H.W. helped to analyze the energy-level alignment. Y.S. helped to analyze the DFT data. C.D., Z.L., and Y.H. contributed to SCLC and EIS data analyses. I.Z.M., E.G.L., L. Yang, and Cezhou Zhao contribute to the revision of the original manuscript. L. Yin, with the help of Chun Zhao and C.-Q.M. designed the experiment and wrote the manuscript. All authors contributed to the interpretation and discussion of the results.

## DECLARATION OF INTERESTS

The authors declare no conflicts of interest.

Received: February 23, 2022

Revised: April 6, 2022

Accepted: April 29, 2022

Published: May 23, 2022

## REFERENCES

- Jiang, Q., Zhao, Y., Zhang, X., Yang, X., Chen, Y., Chu, Z., Ye, Q., Li, X., Yin, Z., and You, J. (2019). Surface passivation of perovskite film for efficient solar cells. *Nat. Photon.* 13, 460–466. <https://doi.org/10.1038/s41566-019-0398-2>.
- Wang, S., Jiang, Y., Juarez-Perez, E.J., Ono, L.K., and Qi, Y. (2016). Accelerated degradation of methylammonium lead iodide perovskites induced by exposure to iodine vapour. *Nat. Energy* 2, 16195. <https://doi.org/10.1038/nenergy.2016.195>.
- Chen, C., Song, Z., Xiao, C., Zhao, D., Shrestha, N., Li, C., Yang, G., Yao, F., Zheng, X., Ellingson, R.J., et al. (2019). Achieving a high open-circuit voltage in inverted wide-bandgap perovskite solar cells with a graded perovskite homojunction. *Nano Energy* 61, 141–147. <https://doi.org/10.1016/j.nanoen.2019.04.069>.
- Kojima, A., Teshima, K., Shirai, Y., and Miyasaka, T. (2009). Organometal halide perovskites as visible-light sensitizers for photovoltaic cells. *J. Am. Chem. Soc.* 131, 6050–6051. <https://doi.org/10.1021/ja809598r>.
- Im, J.H., Jang, I.H., Pellet, N., Grätzel, M., and Park, N.G. (2014). Growth of CH<sub>3</sub>NH<sub>3</sub>PbI<sub>3</sub> cuboids with controlled size for high-efficiency perovskite solar cells. *Nat. Nanotechnol.* 9, 927–932. <https://doi.org/10.1038/nnano.2014.181>.
- National Renewable Energy Laboratory. Best research-cell efficiency chart. <https://www.nrel.gov/pv/cell-efficiency.html>.
- Liu, X., Zhang, Y., Shi, L., Liu, Z., Huang, J., Yun, J.S., Zeng, Y., Pu, A., Sun, K., Hameiri, Z., et al. (2018). Exploring inorganic binary alkaline halide to passivate defects in low-temperature-processed planar-structure hybrid perovskite solar cells. *Adv. Energy Mater.* 8, 1800138. <https://doi.org/10.1002/aenm.201800138>.
- Wang, P., Jiang, Q., Zhao, Y., Chen, Y., Chu, Z., Zhang, X., Zhou, Y., and You, J. (2018). Synergistic improvement of perovskite film quality for efficient solar cells via multiple chloride salt additives. *Sci. Bull.* 63, 726–731. <https://doi.org/10.1016/j.scib.2018.05.003>.
- Wei, J., Guo, F., Wang, X., Xu, K., Lei, M., Liang, Y., Zhao, Y., and Xu, D. (2018). SnO<sub>2</sub>-in-Polymer matrix for high-efficiency perovskite solar cells with improved reproducibility and stability. *Adv. Mater.* 30, e1805153. <https://doi.org/10.1002/adma.201805153>.
- You, J., Hong, Z., Yang, Y.M., Chen, Q., Cai, M., Song, T.-B., Chen, C.-C., Lu, S., Liu, Y., Zhou, H., and Yang, Y. (2014). Low-temperature solution-processed perovskite solar cells with high efficiency and flexibility. *ACS Nano* 8, 1674–1680. <https://doi.org/10.1021/nm406020d>.
- Xiong, L., Guo, Y., Wen, J., Liu, H., Yang, G., Qin, P., and Fang, G. (2018). Review on the application of SnO<sub>2</sub> in perovskite solar cells. *Adv. Funct. Mater.* 28, 1802757. <https://doi.org/10.1002/adfm.201802757>.
- Yoo, J.J., Seo, G., Chua, M.R., Park, T.G., Lu, Y., Rotermund, F., Kim, Y.-K., Moon, C.S., Jeon, N.J., Correa-Baena, J.-P., et al. (2021). Efficient perovskite solar cells via improved carrier management. *Nature* 590, 587–593. <https://doi.org/10.1038/s41586-021-03285-w>.
- Aygüler, M.F., Hufnagel, A.G., Rieder, P., Wussler, M., Jaegermann, W., Bein, T., Dyakonov, V., Petrus, M.L., Baumann, A., and Docampo, P. (2018). Influence of Fermi level alignment with tin oxide on the hysteresis of perovskite solar cells. *ACS Appl. Mater. Inter.* 10, 11414–11419. <https://doi.org/10.1021/acsami.8b00990>.

14. Yang, D., Yang, R., Wang, K., Wu, C., Zhu, X., Feng, J., Ren, X., Fang, G., Priya, S., and Liu, S. (2018). High efficiency planar-type perovskite solar cells with negligible hysteresis using EDTA-complexed SnO<sub>2</sub>. *Nat. Commun.* **9**, 3239. <https://doi.org/10.1038/s41467-018-05760-x>.
15. Zhu, P., Gu, S., Luo, X., Gao, Y., Li, S., Zhu, J., and Tan, H. (2019). Simultaneous contact and grain-boundary passivation in planar perovskite solar cells using SnO<sub>2</sub>-KCl composite electron transport layer. *Adv. Energy Mater.* **10**, 1903083. <https://doi.org/10.1002/aenm.201903083>.
16. Altinkaya, C., Aydin, E., Ugur, E., Isikgor, F.H., Subbiah, A.S., De Bastiani, M., Liu, J., Babayigit, A., Allen, T.G., Laquai, F., et al. (2021). Tin oxide electron-selective layers for efficient, stable, and scalable perovskite solar cells. *Adv. Mater.* **33**, 2005504. <https://doi.org/10.1002/adma.202005504>.
17. Krückemeier, L., Rau, U., Stolterfoht, M., and Kirchartz, T. (2020). How to report record open-circuit voltages in lead-halide perovskite solar cells. *Adv. Energy Mater.* **10**, 1902573. <https://doi.org/10.1002/aenm.201902573>.
18. Park, M., Kim, J.-Y., Son, H.-J., Lee, C.-H., Jang, S.S., and Ko, M.J. (2016). Low-temperature solution-processed Li-doped SnO<sub>2</sub> as an effective electron transporting layer for high-performance flexible and wearable perovskite solar cells. *Nano Energy* **26**, 208–215. <https://doi.org/10.1016/j.nanoen.2016.04.060>.
19. Wang, E., Chen, P., Yin, X., Wu, Y., and Que, W. (2019). Tailoring electronic properties of SnO<sub>2</sub> quantum dots via aluminum addition for high-efficiency perovskite solar cells. *Sol. RRL* **3**, 1900041. <https://doi.org/10.1002/solr.201900041>.
20. Halvani Anaraki, E., Kermanpur, A., Mayer, M.T., Steier, L., Ahmed, T., Turren-Cruz, S.-H., Seo, J., Luo, J., Zakeeruddin, S.M., Tress, W.R., et al. (2018). Low-temperature Nb-doped SnO<sub>2</sub> electron-selective contact yields over 20% efficiency in planar perovskite solar cells. *ACS Energy Lett.* **3**, 773–778. <https://doi.org/10.1021/acscenergylett.8b00055>.
21. Chen, J., Zhao, X., Kim, S.-G., and Park, N.-G. (2019). Multifunctional chemical linker imidazoleacetic acid hydrochloride for 21% efficient and stable planar perovskite solar cells. *Adv. Mater.* **31**, 1902902. <https://doi.org/10.1002/adma.201902902>.
22. Yang, G., Wang, C., Lei, H., Zheng, X., Qin, P., Xiong, L., Zhao, X., Yan, Y., and Fang, G. (2017). Interface engineering in planar perovskite solar cells: energy level alignment, perovskite morphology control and high performance achievement. *J. Mater. Chem. A* **5**, 1658–1666. <https://doi.org/10.1039/c6ta08783c>.
23. Dai, Z., Yadavalli, S.K., Chen, M., Abbaspourtamijani, A., Qi, Y., and Padture, N.P. (2021). Interfacial toughening with self-assembled monolayers enhances perovskite solar cell reliability. *Science* **372**, 618–622. <https://doi.org/10.1126/science.abf5602>.
24. Lee, Y., Paek, S., Cho, K.T., Oveisi, E., Gao, P., Lee, S., Park, J.-S., Zhang, Y., Humphry-Baker, R., Asiri, A.M., and Nazeeruddin, M.K. (2017). Enhanced charge collection with passivation of the tin oxide layer in planar perovskite solar cells. *J. Mater. Chem. A* **5**, 12729–12734. <https://doi.org/10.1039/c7ta04128d>.
25. Ke, W., Zhao, D., Xiao, C., Wang, C., Cimaroli, A.J., Grice, C.R., Yang, M., Li, Z., Jiang, C.-S., Al-Jassim, M., et al. (2016). Cooperative tin oxide fullerene electron selective layers for high-performance planar perovskite solar cells. *J. Mater. Chem. A* **4**, 14276–14283. <https://doi.org/10.1039/c6ta05095f>.
26. Ma, J., Yang, G., Qin, M., Zheng, X., Lei, H., Chen, C., Chen, Z., Guo, Y., Han, H., Zhao, X., and Fang, G. (2017). MgO nanoparticle modified anode for highly efficient SnO<sub>2</sub>-based planar perovskite solar cells. *Adv. Sci.* **4**, 1700031. <https://doi.org/10.1002/advs.201700031>.
27. Cao, Q., Li, Z., Han, J., Wang, S., Zhu, J., Tang, H., Li, X., and Li, X. (2019). Electron transport bilayer with cascade energy alignment for efficient perovskite solar cells. *Sol. RRL* **3**, 1900333. <https://doi.org/10.1002/solr.201900333>.
28. Tian, C., Lin, K., Lu, J., Feng, W., Song, P., Xie, L., and Wei, Z. (2020). Interfacial bridge using a cis-fulleropyrrolidine for efficient planar perovskite solar cells with enhanced stability. *Small Methods* **4**, 1900476. <https://doi.org/10.1002/smtd.201900476>.
29. Naguib, M., Kurtoglu, M., Presser, V., Lu, J., Niu, J., Heon, M., Hultman, L., Gogotsi, Y., and Barsoum, M.W. (2011). Two-dimensional nanocrystals produced by exfoliation of Ti<sub>3</sub>AlC<sub>2</sub>. *Adv. Mater.* **23**, 4248–4253. <https://doi.org/10.1002/adma.201102306>.
30. Xu, H., Ren, A., Wu, J., and Wang, Z. (2020). Recent advances in 2D MXenes for photodetection. *Adv. Funct. Mater.* **30**, 2000907. <https://doi.org/10.1002/adfm.202000907>.
31. Naguib, M., Mashtalir, O., Carle, J., Presser, V., Lu, J., Hultman, L., Gogotsi, Y., and Barsoum, M.W. (2012). Two-dimensional transition metal carbides. *ACS Nano* **6**, 1322–1331. <https://doi.org/10.1021/nn204153h>.
32. Naguib, M., Halim, J., Lu, J., Cook, K.M., Hultman, L., Gogotsi, Y., and Barsoum, M.W. (2013). New two-dimensional niobium and vanadium carbides as promising materials for Li-ion batteries. *J. Am. Chem. Soc.* **135**, 15966–15969. <https://doi.org/10.1021/ja405735d>.
33. Anasori, B., Xie, Y., Beidaghi, M., Lu, J., Hosler, B.C., Hultman, L., Kent, P.R.C., Gogotsi, Y., and Barsoum, M.W. (2015). Two-dimensional, ordered, double transition metals carbides (MXenes). *ACS Nano* **9**, 9507–9516. <https://doi.org/10.1021/acsnano.5b03591>.
34. Ghidoui, M., Lukatskaya, M.R., Zhao, M.Q., Gogotsi, Y., and Barsoum, M.W. (2014). Conductive two-dimensional titanium carbide 'clay' with high volumetric capacitance. *Nature* **516**, 78–81. <https://doi.org/10.1038/nature13970>.
35. Guo, Z., Gao, L., Xu, Z., Teo, S., Zhang, C., Kamata, Y., Hayase, S., and Ma, T. (2018). High electrical conductivity 2D MXene serves as additive of perovskite for efficient solar cells. *Small* **14**, 1802738. <https://doi.org/10.1002/smll.201802738>.
36. Zhou, Q., Duan, J., Du, J., Guo, Q., Zhang, Q., Yang, X., Duan, Y., and Tang, Q. (2021). Tailored lattice "Tape" to confine Tensile interface for 11.08%-efficiency all-inorganic CsPbBr<sub>3</sub> perovskite solar cell with an ultrahigh voltage of 1.702 V. *Adv. Sci.* **8**, 2101418. <https://doi.org/10.1002/advs.202101418>.
37. Yang, L., Dall'Agnese, Y., Hantanasirisakul, K., Shuck, C.E., Maleski, K., Alhabeb, M., Chen, G., Gao, Y., Sanehira, Y., Jena, A.K., et al. (2019). SnO<sub>2</sub>-Ti<sub>3</sub>C<sub>2</sub> MXene electron transport layers for perovskite solar cells. *J. Mater. Chem. A* **7**, 5635–5642. <https://doi.org/10.1039/c8ta12140k>.
38. Agresti, A., Pazniak, A., Pescetelli, S., Di Vito, A., Rossi, D., Pecchia, A., der Maur, M.A., Liedl, A., Larciprete, R., Kuznetsov, D.V., et al. (2019). Author Correction: titanium-carbide MXenes for work function and interface engineering in perovskite solar cells. *Nat. Mater.* **18**, 1264. <https://doi.org/10.1038/s41563-019-0527-9>.
39. Huang, L., Zhou, X., Xue, R., Xu, P., Wang, S., Xu, C., Zeng, W., Xiong, Y., Sang, H., and Liang, D. (2020). Low-temperature growing anatase TiO<sub>2</sub>/SnO<sub>2</sub> multi-dimensional heterojunctions at MXene conductive network for high-efficient perovskite solar cells. *Nano-Micro Lett.* **12**, 44. <https://doi.org/10.1007/s40820-020-0379-5>.
40. Hou, C., and Yu, H. (2021). ZnO/Ti<sub>3</sub>C<sub>2</sub>T<sub>x</sub> monolayer electron transport layers with enhanced conductivity for highly efficient inverted polymer solar cells. *Chem. Eng. J.* **407**, 127192. <https://doi.org/10.1016/j.cej.2020.127192>.
41. Jin, X., Yang, L., and Wang, X.F. (2021). Efficient two-dimensional perovskite solar cells realized by incorporation of Ti<sub>3</sub>C<sub>2</sub>T<sub>x</sub> MXene as nanodopants. *Nano Micro Lett.* **13**, 68. <https://doi.org/10.1007/s40820-021-00602-w>.
42. Li, Z., Wang, P., Ma, C., Igbari, F., Kang, Y., Wang, K.L., Song, W., Dong, C., Li, Y., Yao, J., et al. (2021). Single-layered MXene nanosheets doping TiO<sub>2</sub> for efficient and stable double perovskite solar cells. *J. Am. Chem. Soc.* **143**, 2593–2600. <https://doi.org/10.1021/jacs.0c12739>.
43. Yang, Y., Lu, H., Feng, S., Yang, L., Dong, H., Wang, J., Tian, C., Li, L., Lu, H., Jeong, J., et al. (2021). Modulation of perovskite crystallization processes towards highly efficient and stable perovskite solar cells with MXene quantum dot-modified SnO<sub>2</sub>. *Energy Environ. Sci.* **14**, 3447–3454. <https://doi.org/10.1039/d1ee00056j>.
44. Wang, J., Cai, Z., Lin, D., Chen, K., Zhao, L., Xie, F., Su, R., Xie, W., Liu, P., and Zhu, R. (2021). Plasma oxidized Ti<sub>3</sub>C<sub>2</sub>T<sub>x</sub> MXene as electron transport layer for efficient perovskite solar cells. *ACS Appl. Mater. Inter.* **13**, 32495–32502.
45. Chen, T., Tong, G., Xu, E., Li, H., Li, P., Zhu, Z., Tang, J., Qi, Y., and Jiang, Y. (2019). Accelerating hole extraction by inserting 2D Ti<sub>3</sub>C<sub>2</sub>-MXene interlayer to all inorganic perovskite solar cells with long-term stability. *J. Mater. Chem. A* **7**, 20597–20603. <https://doi.org/10.1039/c9ta06035a>.
46. Yang, L., Dall'Agnese, C., Dall'Agnese, Y., Chen, G., Gao, Y., Sanehira, Y., Jena, A.K., Wang, X.-F., Gogotsi, Y., and Miyasaka, T. (2019). Surface-modified metallic Ti<sub>3</sub>C<sub>2</sub>T<sub>x</sub> MXene as electron transport layer for planar heterojunction perovskite solar cells. *Adv.*

- Funct. Mater. 29, 1905694. <https://doi.org/10.1002/adfm.201905694>.
47. Chen, X., Xu, W., Ding, N., Ji, Y., Pan, G., Zhu, J., Zhou, D., Wu, Y., Chen, C., and Song, H. (2020). Dual interfacial modification engineering with 2D MXene quantum dots and copper sulphide nanocrystals enabled high-performance perovskite solar cells. *Adv. Funct. Mater.* 30, 2003295. <https://doi.org/10.1002/adfm.202003295>.
  48. Yang, L., Kan, D., Dall'Agnese, C., Dall'Agnese, Y., Wang, B., Jena, A.K., Wei, Y., Chen, G., Wang, X.-F., Gogotsi, Y., and Miyasaka, T. (2021). Performance improvement of MXene-based perovskite solar cells upon property transition from metallic to semiconductive by oxidation of Ti<sub>3</sub>C<sub>2</sub>T<sub>x</sub> in air. *J. Mater. Chem. A* 9, 5016–5025. <https://doi.org/10.1039/d0ta11397b>.
  49. Wang, Y., Xiang, P., Ren, A., Lai, H., Zhang, Z., Xuan, Z., Wan, Z., Zhang, J., Hao, X., Wu, L., et al. (2020). MXene-modulated electrode/SnO<sub>2</sub> interface boosting charge transport in perovskite solar cells. *ACS Appl. Mater. Inter.* 12, 53973–53983. <https://doi.org/10.1021/acsmami.0c17338>.
  50. Mi, L., Zhang, Y., Chen, T., Xu, E., and Jiang, Y. (2020). Carbon electrode engineering for high efficiency all-inorganic perovskite solar cells. *RSC Adv.* 10, 12298–12303. <https://doi.org/10.1039/d0ra00288g>.
  51. Riaz, H., Anayee, M., Hantanasirisakul, K., Shamsabadi, A.A., Anasori, B., Gogotsi, Y., and Soroush, M. (2020). Surface modification of a MXene by an aminosilane coupling agent. *Adv. Mater. Inter.* 7, 1902008. <https://doi.org/10.1002/admi.201902008>.
  52. Zhao, J., Yang, Y., Yang, C., Tian, Y., Han, Y., Liu, J., Yin, X., and Que, W. (2018). A hydrophobic surface enabled salt-blocking 2D Ti<sub>3</sub>C<sub>2</sub>MXene membrane for efficient and stable solar desalination. *J. Mater. Chem. A* 6, 16196–16204. <https://doi.org/10.1039/c8ta05569f>.
  53. Chen, W.Y., Lai, S.N., Yen, C.C., Jiang, X., Peroulis, D., and Stanciu, L.A. (2020). Surface functionalization of Ti<sub>3</sub>C<sub>2</sub>T<sub>x</sub> MXene with highly reliable superhydrophobic protection for volatile organic compounds sensing. *ACS Nano* 14, 11490–11501. <https://doi.org/10.1021/acsnano.0c03896>.
  54. Khazaei, M., Arai, M., Sasaki, T., Ranjbar, A., Liang, Y., and Yunoki, S. (2015). OH-terminated two-dimensional transition metal carbides and nitrides as ultralow work function materials. *Phys. Rev. B* 92, 075411. <https://doi.org/10.1103/physrevb.92.075411>.
  55. Halim, J., Cook, K.M., Naguib, M., Eklund, P., Gogotsi, Y., Rosen, J., and Barsoum, M.W. (2016). X-ray photoelectron spectroscopy of select multi-layered transition metal carbides (MXenes). *Appl. Surf. Sci.* 362, 406–417. <https://doi.org/10.1016/j.apsusc.2015.11.089>.
  56. Shah, S.A., Habib, T., Gao, H., Gao, P., Sun, W., Green, M.J., and Radovic, M. (2017). Template-free 3D titanium carbide (Ti<sub>3</sub>C<sub>2</sub>T<sub>x</sub>) MXene particles crumpled by capillary forces. *ChemComm* 53, 400–403. <https://doi.org/10.1039/c6cc07733a>.
  57. Yoo, D., Kim, Y., Min, M., Ahn, G.H., Lien, D.-H., Jang, J., Jeong, H., Song, Y., Chung, S., Javey, A., and Lee, T. (2018). Highly reliable superhydrophobic protection for organic field-effect transistors by fluoroalkylsilane-coated TiO<sub>2</sub> nanoparticles. *ACS Nano* 12, 11062–11069. <https://doi.org/10.1021/acsnano.8b05224>.
  58. Ren, C.E., Zhao, M.-Q., Makaryan, T., Halim, J., Boota, M., Kota, S., Anasori, B., Barsoum, M.W., and Gogotsi, Y. (2016). Porous two-dimensional transition metal carbide (MXene) flakes for high-performance Li-ion storage. *ChemElectroChem* 3, 689–693. <https://doi.org/10.1002/celec.201600059>.
  59. Liu, Y.-T., Zhang, P., Sun, N., Anasori, B., Zhu, Q.-Z., Liu, H., Gogotsi, Y., and Xu, B. (2018). Self-assembly of transition metal oxide nanostructures on MXene nanosheets for fast and stable lithium storage. *Adv. Mater.* 30, 1707334. <https://doi.org/10.1002/adma.201707334>.
  60. Liu, Z., Qiu, L., Ono, L.K., He, S., Hu, Z., Jiang, M., Tong, G., Wu, Z., Jiang, Y., Son, D.-Y., et al. (2020). A holistic approach to interface stabilization for efficient perovskite solar modules with over 2,000-hour operational stability. *Nat. Energy* 5, 596–604. <https://doi.org/10.1038/s41560-020-0653-2>.
  61. Jung, M., Ji, S.-G., Kim, G., and Seok, S.I. (2019). Perovskite precursor solution chemistry: from fundamentals to photovoltaic applications. *Chem. Soc. Rev.* 48, 2011–2038. <https://doi.org/10.1039/c8cs00656c>.
  62. Bi, C., Wang, Q., Shao, Y., Yuan, Y., Xiao, Z., and Huang, J. (2015). Non-wetting surface-driven high-aspect-ratio crystalline grain growth for efficient hybrid perovskite solar cells. *Nat. Commun.* 6, 7747. <https://doi.org/10.1038/ncomms8747>.
  63. Kim, M., Kim, G.-H., Lee, T.K., Choi, I.W., Choi, H.W., Jo, Y., Yoon, Y.J., Kim, J.W., Lee, J., Huh, D., et al. (2019). Methylammonium chloride induces intermediate phase stabilization for efficient perovskite solar cells. *Joule* 3, 2179–2192. <https://doi.org/10.1016/j.joule.2019.06.014>.
  64. Xiong, Z., Lan, L., Wang, Y., Lu, C., Qin, S., Chen, S., Zhou, L., Zhu, C., Li, S., Meng, L., et al. (2021). Multifunctional polymer framework modified SnO<sub>2</sub> enabling a photostable  $\alpha$ -FAPbI<sub>3</sub> perovskite solar cell with efficiency exceeding 23%. *ACS Energy Lett.* 6, 3824–3830. <https://doi.org/10.1021/acsenenergylett.1c01763>.
  65. Rühle, S. (2016). Tabulated values of the Shockley–Queisser limit for single junction solar cells. *Solar Energy* 130, 139–147. <https://doi.org/10.1016/j.solener.2016.02.015>.
  66. Liu, J., Shen, X., Zhou, J., Wang, M., Niu, C., Qian, T., and Yan, C. (2019). Nonflammable and high-voltage-tolerated polymer electrolyte achieving high stability and safety in 4.9 V-Class lithium metal battery. *ACS Appl. Mater. Inter.* 11, 45048–45056. <https://doi.org/10.1021/acsmami.9b14147>.
  67. Zhang, Z., Hu, L., Wu, H., Weng, W., Koh, M., Redfern, P.C., Curtiss, L.A., and Amine, K. (2013). Fluorinated electrolytes for 5 V lithium-ion battery chemistry. *Energy Environ. Sci.* 6, 1806–1810. <https://doi.org/10.1039/c3ee24414h>.
  68. Dong, Q., Li, J., Shi, Y., Chen, M., Ono, L.K., Zhou, K., Zhang, C., Qi, Y., Zhou, Y., Padture, N.P., and Wang, L. (2019). Improved SnO<sub>2</sub> electron transport layers solution-deposited at near room temperature for rigid or flexible perovskite solar cells with high efficiencies. *Adv. Energy Mater.* 9, 1900834. <https://doi.org/10.1002/aenm.201900834>.
  69. You, J., Si, C., Zhou, J., and Sun, Z. (2019). Contacting MoS<sub>2</sub> to MXene: vanishing p-type Schottky barrier and enhanced hydrogen evolution catalysis. *J. Phys. Chem. C* 123, 3719–3726. <https://doi.org/10.1021/acs.jpcc.8b12469>.
  70. Shi, D., Adinolfi, V., Comin, R., Yuan, M., Alarousu, E., Buin, A., Chen, Y., Hoogland, S., Rothenberger, A., Katsiev, K., et al. (2015). Low trap-state density and long carrier diffusion in organolead trihalide perovskite single crystals. *Science* 347, 519–522. <https://doi.org/10.1126/science.aaa2725>.
  71. Liu, Y., Sun, J., Yang, Z., Yang, D., Ren, X., Xu, H., Yang, Z., and Liu, S.F. (2016). 20-mm-Large single-crystalline formamidinium-perovskite wafer for mass production of integrated photodetectors. *Adv. Opt. Mater.* 4, 1829–1837. <https://doi.org/10.1002/adom.201600327>.
  72. Green, M.A. (1981). *Solar Cells: Operating Principles, Technology and System Applications*.
  73. Tumen-Ulzii, G., Qin, C., Klotz, D., Leyden, M.R., Wang, P., Auffray, M., Fujihara, T., Matsushima, T., Lee, J.-W., Lee, S.-J., et al. (2020). Detrimental effect of unreacted PbI<sub>2</sub> on the long-term stability of perovskite solar cells. *Adv. Mater.* 32, 1905035. <https://doi.org/10.1002/adma.201905035>.
  74. Domanski, K., Roose, B., Matsui, T., Saliba, M., Turren-Cruz, S.-H., Correa-Baena, J.-P., Carmona, C.R., Richardson, G., Foster, J.M., De Angelis, F., et al. (2017). Migration of cations induces reversible performance losses over day/night cycling in perovskite solar cells. *Energy Environ. Sci.* 10, 604–613. <https://doi.org/10.1039/c6ee03352k>.
  75. Liu, C., Zhao, Y., Yi, R., Wu, H., Yang, W., Li, Y., Mitrovic, I., Taylor, S., Chalker, P., Liu, R., and Yang, L. (2020). Enhanced electrochemical performance by GeO<sub>x</sub>-Coated MXene nanosheet anode in lithium-ion batteries. *Electrochim. Acta* 358, 136923. <https://doi.org/10.1016/j.electacta.2020.136923>.
  76. Ding, C., Yin, L., Zhang, L., Huang, R., Fan, S., Luo, Q., Lin, J., Li, F., Zhao, C., Osterbacka, R., and Ma, C.-Q. (2021). Revealing the mechanism behind the catastrophic failure of n-i-p type perovskite solar cells under operating conditions and how to suppress it. *Adv. Funct. Mater.* 31, 2103820. <https://doi.org/10.1002/adfm.202103820>.